Metal–Organic Frameworks

International Edition: DOI: 10.1002/anie.201813634
German Edition: DOI: 10.1002/ange.201813634

Stable Hierarchical Bimetal–Organic Nanostructures as High-Performance Electrocatalysts for the Oxygen Evolution Reaction

Wei Zhou[+], Dan-Dan Huang[+], Ya-Pan Wu, Jun Zhao, Tao Wu, Jian Zhang, Dong-Sheng Li, Chenghua Sun,* Pingyun Feng, and Xianhui Bu**

Abstract: *The integration of heterometallic units and nanostructures into metal–organic frameworks (MOFs) used for the oxygen evolution reaction (OER) can enhance the electrocatalytic performance and help elucidate underlying mechanisms. We have synthesized a series of stable MOFs (CTGU-10a1–d1) based on trinuclear metal carboxylate clusters and a hexadentate carboxylate ligand with a (6,6)-connected nia net. We also present a strategy to synthesize hierarchical bimetallic MOF nanostructures (CTGU-10a2–d2). Among these, CTGU-10c2 is the best material for the OER, with an overpotential of 240 mV at a current density of 10 mA cm^{-2} and a Tafel slope of 58 mV dec^{-1}. This is superior to RuO_2 and confirms CTGU-10c2 as one of the few known high-performing pure-phase MOF-OER electrocatalysts. Notably, bimetallic CTGU-10b2 and c2 show an improved OER activity over monometallic CTGU-10a2 and d2. Both DFT and experiments show that the remarkable OER performance of CTGU-10c2 is due to the presence of unsaturated metal sites, a hierarchical nanobelt architecture, and the Ni–Co coupling effect.*

The oxygen evolution reaction plays a critical role in the electrochemical splitting of water.[1–3] Desirable electrocatalysts should not only accelerate the anodic OER, but also have a long-term stability.[4,5] Given the high cost of noble-metal catalysts for large-scale applications,[6] it remains a challenge to synthesize low-cost electrocatalysts with high performance and stability.[7–9] Some successes have been achieved using mixed-transition-metal-based electrocatalysts because of their attractive electrical conductivity, synergistic effect of polymetal atoms, and stability.[10–13] For example, Zhang et al. developed high-performance bimetallic MOF–OER electrocatalysts using a modular synthesis method.[14,15] Moreover, trimetallic-MOF electrocatalysts have also been explored.[16,17] For example, Lan's group reported the NNU-23 electrocatalyst with excellent OER performance.[16]

MOFs have received increasing attention for energy-related applications which benefit from their tunable porosity, high surface area, and diversity in functional species of metal centers and organic linkers.[18–21] However, the low conductivity, small mass permeability, and chemical stability limit their utilization as electrocatalysts.[22–26] To address these issues, one effective strategy is to convert traditional bulk MOF crystals into 2D nanosheets or to grow ultrathin MOF nanosheet arrays on highly conductive substrates.[27–37] A notable example is the study by Zhang et al. in which metal–organic 2D materials are synthesized by an electrochemical/chemical exfoliation strategy and show improved OER performances.[37] Separately, Huang's group combined 2D MOF nanosheets with electrically conductive 2D $Ti_3C_2T_x$ nanosheets, resulting in an improved OER performance.[31] These advances can be ascribed to desirable merits of 2D nanomaterials such as high percentages of exposed active sites, tunable surface atomic structures, and nanometer thickness that ensures rapid mass transport and charge transfer.

Very recently, heterometal units have been introduced into MOF nanostructures, leading to a high OER performance. For instance, Tang's group reported NiCo bimetal–organic framework nanosheets with high electrocatalytic activity towards the OER and explored precise structure–performance relationships at the atomic level.[29] Furthermore, Zhao's group fabricated ultrathin Fe/Ni-based MOF nanosheets that demonstrated a high electrocatalytic performance towards OER.[30] Thus, heterometallic MOF nanosheets are ideal platforms for exploring structure–performance relationships in rational catalyst design at the atomic level.

Currently, reported nanosheets synthesized by sonication exfoliation often encounter problems such as intrinsic restacking and low yield.[38] One way to deal with this problem is to design hierarchical nanostructures.[39] Therefore, the synthesis of low-cost bimetallic hierarchical nanostructured MOFs is highly desirable because of their unique

[*] W. Zhou,[+] D.-D. Huang,[+] Dr. Y. P. Wu, Prof. Dr. J. Zhao, Prof. Dr. T. Wu, Prof. Dr. J. Zhang, Prof. Dr. D.-S. Li
College of Materials and Chemical Engineering, Hubei Provincial Collaborative Innovation Center for New Energy Microgrid, Key Laboratory of Inorganic Nonmetallic Crystalline and Energy Conversion Materials, China Three Gorges University
No. 8, Daxue Road, Yichang, 443002 (China)
E-mail: lidongsheng1@126.com
Prof. Dr. C. Sun
Department of Chemistry and Biotechnology, Faculty of Science, Engineering and Technology, Swinburne University of Technology
Hawthorn VIC 3122 (Australia)
E-mail: chenghuasun@swin.edu.au
Prof. Dr. P. Feng
Department of Chemistry, University of California
Riverside, CA 92521 (USA)
Prof. Dr. X. Bu
Department of Chemistry and Biochemistry, California State University Long Beach
1250 Bellflower Boulevard, Long Beach, CA 90840 (USA)
E-mail: xianhui.bu@csulb.edu
[+] These authors contributed equally to this work.
Supporting information and the ORCID identification number(s) for the author(s) of this article can be found under: https://doi.org/10.1002/anie.201813634.

morphology, different surface atomic structures, highly exposed metal sites, and improved performance.[40]

Herein, we report a series of novel isostructural transition-metal MOFs $[NH_2(CH_3)_2][M_3(\mu_3\text{-}OH)(H_2O)_3(BHB)]$ ($M_3 = Co_3$, Co_2Ni, $CoNi_2$, Ni_3; named CTGU-10a1, b1, c1, d1, respectively) constructed from the hexacarboxylic acid 4,4′,4″-benzene-1,3,5-triyl-hexabenzoic acid (H_6BHB). Moreover, corresponding hierarchical nanostructures (CTGU-10a2–d2) were prepared by controlling the ratio of metal salts in the solvothermal synthesis. Hierarchical CTGU-10c2 ($CoNi_2$-MOF) nanobelts exhibit superior electrocatalytic OER performances with a low overpotential of 240 mV at 10 mA cm^{-2}, a small Tafel slope of 58 mV dec^{-1} and a long-term stability of >50 h in an alkaline medium. The OER performance is superior to commercial RuO_2 and is among the best pure-MOF OER electrocatalysts.

Since CTGU-10a1–d1 are isostructural, only CTGU-10a1 is discussed below. Single-crystal X-ray analysis shows that CTGU-10a1 crystallizes in the hexagonal space group $P\bar{6}2c$ (Supporting Information, Table S2). As shown in Figure 1a, CTGU-10a1 adopts a $Co_3(\mu_3\text{-}OH)$ cluster as its secondary

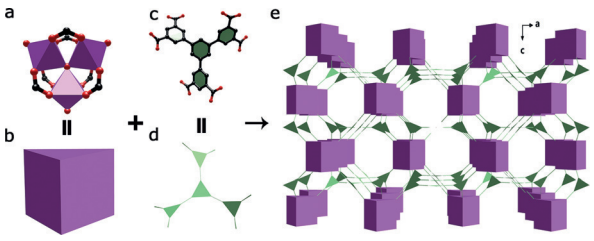

Figure 1. a) Metal trimers in CTGU-10a1 (C: black, O: red, Co: purple). b) Polyhedral representation of the trigonal prismatic geometry. c) Structure of the BHB ligand. d) Hexatopic BHB ligand. e) Framework of the nia topology.

building unit (SBU, Figure 1b). Each trinuclear cluster contains three Co^{II} ions and a μ_3-OH and is coordinated by six carboxylate groups and three H_2O molecules (Supporting Information, Figure S1a). Each BHB^{6-} linker is also connected to six $M_3(\mu_3\text{-}OH)$ clusters, forming a 3D porous framework as a (6,6)-c nia network (Figure 1e) with a guest-accessible volume of 43.8% as calculated using PLATON.

Different CTGU-10 samples were prepared by similar solvothermal synthesis. Interstingly, the morphology of the crystallite changed with the Co/Ni ratio. At a ratio of 3:0, CTGU-10a1 forms a hexagonal bipyramidal structure (Supporting Information, Figures S3a,b) at 2:1, CTGU-10b1 (Co_2Ni-MOF) shows a spindle shape (Figures S3c,d), at 1:2, CTGU-10c1 ($CoNi_2$-MOF) becomes partially spindle-shaped and appears strip-like (Figures S3e,f), and at 0:3, CTGU-10d1 is spindle-like as well (Figures S3g,h and Table S1).

Since the morphology and microstructure of materials have great influence on their properties, we further studied the method of synthesis of the MOF bulk. A series of CTGU-10 powder materials were obtained by increasing the concentration of linker and metal salts. As shown in Figure S9 (Supporting Information), the X-ray diffraction patterns of CTGU-10 bulk and powder samples are in good agreement with the simulated patterns, which confirms their purity. One interesting finding is that CTGU-10 powder features hierarchical nanostructures (nanobelts and nanospheres) that originate from the assembly of nanosheets. At a Co/Ni ratio of 3:0, CTGU-10a2 takes the form of nanospheres assembled by nanosheets (Figure 2a). The diameter of those hierarchical

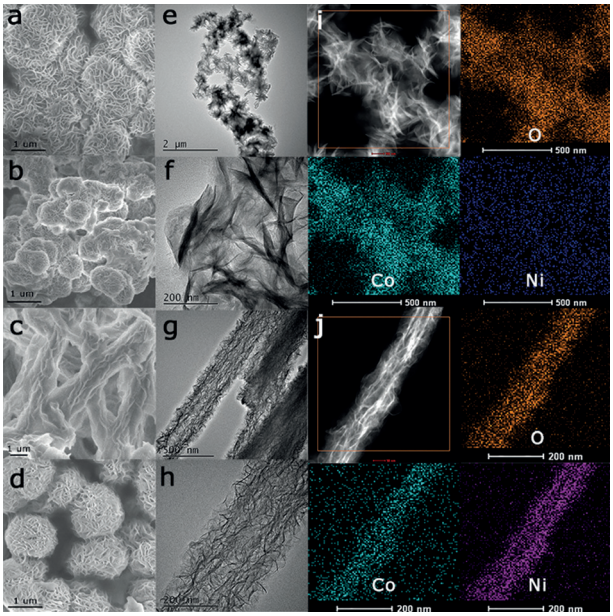

Figure 2. SEM images of a) CTGU-10a2, b) CTGU-10b2, c) CTGU-10c2, and d) CTGU-10d2; e),f) High-resolution TEM images of CTGU-10b2; g),h) High-resolution TEM images of CTGU-10c2; i),j) HAADF-TEM images and TEM-EDS mapping images of i) CTGU-10b2 and j) CTGU-10c2.

nanospheres is about 1.44 μm (Supporting Information, Figure S12a). At a Co/Ni ratio of 2:1, CTGU-10b2 (Co_2Ni-MOF) also adopts hierarchical nanospheres (Figures 2b,e,f) that are assembled from nanosheets. The thickness of the nanosheets is about 1.11 nm (Supporting Information, Figure S11b) and the diameter of the nanospheres is about 1.83 μm (Figure S12b). At a ratio of 1:2, CTGU-10c2 ($CoNi_2$-MOF) forms hierarchical nanobelts constructed from nanosheets (Figures 2c,g,h). The thickness of the nanosheets is about 1.03 or 1.05 nm (Supporting Information, Figure S11a) and the width of the nanobelts is about 1.11 μm (Figure S12c). At a Co/Ni ratio of 0:3, CTGU-10d2 (Ni_3-MOF) shows hierarchical nanospheres (Figure 2d). The diameter of those nanospheres is about 1.44 μm (Supporting Information, Figure S12d). Such a phenomenon may be related to the ligand used in the solvothermal synthesis, making it possible to tune the crystalline morphology by adjusting the molar ratio of the metal salts. This method may open up a new way for the synthesis of hierarchical MOF nanostructures.

Moreover, energy dispersive spectroscopy mapping (EDS, Figure 2j and Supporting Information, Figure S10), inductively coupled plasma-mass spectrometry (ICP, Table S3), and XPS measurements were performed to explore the composition of the hierarchical nanobelts in CTGU-10c2 and the element content of Co and Ni. Figure 2j shows that both

elements are distributed uniformly on the surfaces of the Co/Ni-MOF nanobelts. ICP reveals that CTGU-10c2 contains 7.84 % Co and 13.6 % Ni. Both EDS and ICP results suggest that the Co/Ni molar ratio is close to 1:2. The survey XPS spectrum (Supporting Information, Figure S5) suggests that CTGU-10c2 contains Co, Ni, C, O, and N species. Additionally, Tyndall light scattering was performed to explore the dispersity of the prepared nanosheets. The photograph of the Tyndall light scattering shows that CTGU-10a2–d2 can be dispersed in a CH_3OH solution (Figure S8) which exhibits the nature of the nanostructures.

The electrocatalytic evolution of oxygen in the same system was explored in a 0.1 M KOH electrolyte. All data were obtained without iR-correction. First, the bulk samples were modified on a glass carbon electrode after dispersion. The LSV curves, Tafel plots, and electrochemical impedance spectroscopy (EIS) results are shown in Figure 3 a and Figure S13a, b (Supporting Information). As presented in Figure S13 and Tables S4 and S5, CTGU-10b1 and CTGU-10c1 have an overpotential of 400 mV and 390 mV, which is lower than the values of CTGU-10a1 (416 mV), CTGU-10d1 (500 mV), and RuO_2 (320 mV). The corresponding Tafel slopes of CTGU-10a1–d1 and RuO_2 are 102, 95, 87, 140, and 62 mV dec^{-1}, respectively, which suggests that the kinetics of the bimetallic electrocatalysts is more effective in the OER process than that of monometallic electrocatalysts. To further explore the relationship between the atomic structure, the nanolevel morphology, and the high OER performance, the hierarchical nanostructures of CTGU-10a2–d2 were tested in the similar way. As shown in Figure 3 a, CTGU-10c2 surprisingly shows superior OER performances with an onset potential of 140 mV, which is distinctly better than that of CTGU-10a2 (330 mV), CTGU-10b2 (310 mV), and CTGU-10d2 (340 mV), and is even lower than that of commercial RuO_2 (250 mV). The corresponding Tafel slopes for CTGU-10a2–d2 and RuO_2 are 92, 81, 58, 127, and 62 mV dec^{-1}, respectively, which demonstrates that the OER performance of the hierarchical CTGU-10 nanostructures is superior to that of the CTGU-10 bulk materials. Furthermore, the EIS results (Figure 3 d) also show that CTGU-10c2 has the highest electron transfer ability. As shown in Figure 3 e, the polarization curve of CTGU-10c2 remains essentially unchanged even after 1000 cycles, confirming its excellent stability during the electrocatalytic process. Additionally, the *i–t* curves at a current density of 10 mA cm^{-2} show for all materials that the catalyst retains its electrocatalytic activity for at least 50 h (Supporting Information, Figure S14). Conclusively, the electrochemical active surfaces were examined by electrochemical double-layer capacitance (Cdll). Cyclic voltammetry (CV) measurements were performed between 0.39 and 0.49 V at rates varying from 20 to 100 mV s^{-1} (Figure S15). As shown in Figure 3 f, the Cdll of CTGU-10c2, 8.9 mF cm^{-2}, is larger than that of CTGU-10a2 (3.5 mF cm^{-2}), CTGU-10b2 (5.5 mF cm^{-2}), and CTGU-10d2 (1.6 mF cm^{-2}). The results demonstrate that the hierarchical CTGU-10c2 nanobelts are not only highly electrocatalytically active but also stable electrocatalysts for OER.

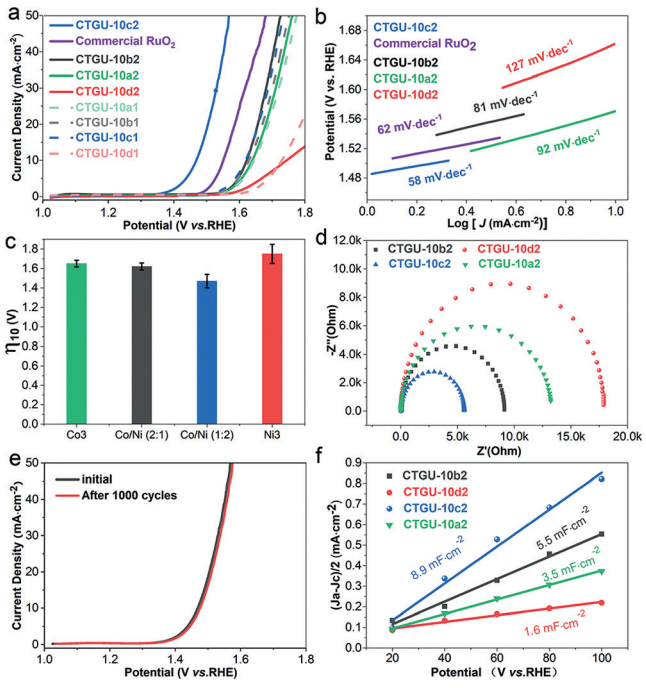

Figure 3. a) LSV curves and b) Tafel plots of RuO_2 and the CTGU electrocatalysts in the OER in 0.1 M KOH. c) Comparison of the overpotential at a current density of 10 mA cm^{-2}. d) Electrochemical impedance spectrum of the CTGU-10a2–d2 catalysts. e) Polarization curves of CTGU-10c2 after zero and 1000 CV cycles. f) Current density difference at 1.47 V vs. scan rate, yielding the double-layer capacitance (Cdll) of the CTGU-10 hierarchical nanostructures.

Furthermore, the Turnover frequency (TOF) was calculated to evaluate the intrinsic activity of the OER electrocatalysts.[43,44] As shown in Figure S16 a, b (Supporting Information), CTGU-10c2 shows a higher TOF value (0.05378 s^{-1}) than the other hierarchical CTGU-10 nanostructures at the given potential of 240 mV (CTGU-10a2: 0.00232 s^{-1}, CTGU-10b2: 0.00338 s^{-1}, CTGU-10d2: 0.00258 s^{-1}). Moreover, the TOF values of the hierarchical CTGU-10 nanostructures are higher than those of the CTGU-10 bulk materials. It is worth noting that no additional conductive materials are added during the OER testing, which shows that the hierarchical nanostructures possess an improved electrical conductivity on their own. More importantly, compared to most reported bimetallic MOF-based electrocatalysts and commercial RuO_2, the bimetallic hierarchical CTGU-10c nanobelts show much better OER performances, which can be attributed to the ultrathin thickness of the nanostructures, the improved electrical conductivity, and the coupling effect between Co and Ni.

In part because of the low chemical stability, as-synthesized MOFs have shown limited electrochemical applications. Many factors, including the testing environment, metal ions, organic ligands, metal–ligand coordination geometry, and hydrophobicity of the pore surface can influence the stability of the MOFs.[32,41,42] The PXRD (powder x-ray diffraction) measurements of the CTGU-10 bulk materials and hierarchical nanostructures after the OER process (Supporting Information, Figure S9 b) show that the CTGU-10 samples are stable. Further FTIR, PXRD, and SEM measurements were done after the samples were immersed in different pH

environments to explore the robustness of the MOF-based electrocatalysts. As is shown in Figure S6a, the FTIR spectra show negligible variance compared with the untreated samples. Figure S9c–f shows that the CTGU-10 samples are stable in a pH range of 12 to 13 for at least 24 h. The SEM measurements (Figure S12) showed that there is no apparent morphological change after immersion in 0.1M KOH, which underlines the relationship between structure and electrocatalytic performance. To further understand the possible variance of the chemical composition on the surfaces and the electronic states of the MOF-based electrocatalysts, XPS measurements of the samples after the OER tests were also done (Figures S4 and S5). After the OER tests, the signals of CTGU-10b2 shift to lower binding energies in the Co 2p spectrum, and to higher binding energies in the Ni 2p spectrum. For CTGU-10c2, the Ni 2p signals shift to lower binding energies, while the Co 2p signals shift to higher binding energies, indicating a partial electron transfer between Co^{2+} and Ni^{2+} through the oxygen of the H_6BHB ligands. These XPS results reveal that the addition of Ni species can change the valence of Co^{2+} and the ability of the material to accept electrons during OER tests, which influences the coupling effect between Ni and Co in bimetallic CTGU-10 electrocatalysts. Similar synergistic effects have been reported in recent studies.[29,36,45] Thus, the catalytic OER performances are enhanced.

To understand the observed performance, especially the coupling effect of Co and Ni, the OER performance of four MOF catalysts with different metal combinations were compared in density functional theory (DFT) calculations. Figure S17a (Supporting Information) shows the simplified model catalyst, focusing on the effect of different combinations of the metals with the same organic ligands. The calculated OER energy profile and overpotenatial are given in Figure S17b. It is found that 1) bimetallic MOFs perform better than single-metal MOFs, 2) Co performs better than Ni, and 3) $CoNi_2$ is the best combination among the four with a calculated overpotential of 420 mV. The improvement associated with the new metal originates from the shift of the d-band center to a higher energy level, as reported in the literature. Such an electronic change occurs due to the slight difference between the Co–O and Ni–O bonds in the bimetallic MOF structures. This is important information for catalyst design, since it allows to choose specific metals or new ligands that cause heavier distortion and further improve the performance. According to our calculations, Co is still the active center in case of the $CoNi_2$ structure, which confirms that the role of the newly introduced Ni center is to cause distortion and thus improve the activity of the Co center. As a result, the $CoNi_2$-MOF performs better than the Co_2Ni-MOF. Therefore, it is recommended that metals with notably different sizes than Co can be considered for further improvement. This is currently under investigation by our team.

In summary, a series of novel bimetal–organic hierarchical nanostructures with high percentages of open metal sites and coordinated water molecules were fabricated by solvothermal synthesis. The OER performances of these hierarchical nanostructures were investigated by DFT calculations and experimental means. The hierarchical CTGU-10c2 nanobelts show an outstanding electrocatalytic performance towards the OER with a lower overpotential of 240 mV at 10 mA cm^{-2} and a small Tafel slope of 58 mV dec^{-1}. The excellent performance demonstrates that hierarchical MOF nanobelts can be highly efficient in the OER and other applications. Importantly, an effective method for the preparation of high-quality and bimetallic hierarchical MOF nanostructures was also developed.

Acknowledgements

This work was supported by the NSF of China (Nos. 21673127, 21671119, 51572152, and 51502155) and the 111 Project of Hubei Province (2018-19-1).

Conflict of interest

The authors declare no conflict of interest.

Keywords: bimetal–organic nanosheets · hierarchical nanostructures · metal–organic frameworks · oxygen evolution reaction

How to cite: *Angew. Chem. Int. Ed.* **2019**, *58*, 4227–4231
Angew. Chem. **2019**, *131*, 4271–4275

[1] I. Roger, M. A. Shipman, M. D. Symes, *Nat. Rev. Chem.* **2017**, *1*, 0003.
[2] J. D. Blakemore, R. H. Crabtree, G. W. Brudvig, *Chem. Rev.* **2015**, *115*, 12974–13005.
[3] S. Geiger, O. Kasian, M. Ledendecker, E. Pizzutilo, M. A. Mingers, W. T. Fu, O. Diaz-Morales, Z. Li, T. Oellers, L. Fruchter, A. Ludwig, K. J. J. Mayrhofer, M. T. M. Koper, S. Cherevko, *Nat. Catal.* **2018**, *1*, 508–515.
[4] Y. Ping, R. J. Nielsen, W. A. Goddard, *J. Am. Chem. Soc.* **2017**, *139*, 149–155.
[5] W. Sun, Z. Wang, W. Q. Zaman, Z. Zhou, L. Cao, X. Q. Gong, J. Yang, *Chem. Commun.* **2018**, *54*, 996–999.
[6] O. Kasian, J. P. Grote, S. Geiger, S. Cherevko, K. J. J. Mayrhofer, *Angew. Chem. Int. Ed.* **2018**, *57*, 2488–2491; *Angew. Chem.* **2018**, *130*, 2514–2517.
[7] C. A. Downes, S. C. Marinescu, *ChemSusChem* **2017**, *10*, 4374–4392.
[8] Y. Qian, I. A. Khan, D. Zhao, *Small* **2017**, *13*, 1701143.
[9] J. Li, R. Guttinger, R. More, F. Song, W. Wan, G. R. Patzke, *Chem. Soc. Rev.* **2017**, *46*, 6124–6147.
[10] B. Y. Guan, L. Yu, X. W. Lou, *Angew. Chem. Int. Ed.* **2017**, *56*, 2386–2389; *Angew. Chem.* **2017**, *129*, 2426–2429.
[11] Z. Fang, L. Peng, Y. Qian, X. Zhang, Y. Xie, J. J. Cha, G. H. Yu, *J. Am. Chem. Soc.* **2018**, *140*, 5241–5247.
[12] C. R. Zhu, A. L. Wang, W. Xiao, D. L. Chao, X. Zhang, N. U. Tiep, S. Chen, J. N. Kang, X. Wang, J. Ding, J. Wang, H. Zhang, H. J. Fan, *Adv. Mater.* **2018**, *30*, 1705516.
[13] Z. Q. Xue, Y. L. Li, Y. W. Zhang, W. Geng, B. M. Jia, J. Tang, S. X. Bao, H. P. Wang, Y. N. Fan, Z. W. Wei, Z. S. Zhang, Z. F. Ke, G. Q. Li, C. Y. Su, *Adv. Energy Mater.* **2018**, *8*, 1801564.
[14] J. Q. Shen, P. Q. Liao, D. D. Zhou, C. T. He, J. X. Wu, W. X. Zhang, J. P. Zhang, X. M. Chen, *J. Am. Chem. Soc.* **2017**, *139*, 1778–1781.
[15] Y. T. Xu, Z. M. Ye, J. W. Ye, L. M. Cao, R. K. Huang, J. X. Wu, D. D. Zhou, X. F. Zhang, C. T. He, J. P. Zhang, X. M. Cheng,

Angew. Chem. Int. Ed. **2019**, *58*, 139 – 143; *Angew. Chem.* **2019**, *131*, 145 – 149.
[16] X. L. Wang, L. Z. Dong, M. Qiao, Y. J. Tang, J. Liu, Y. F. Li, S. L. Li, J. X. Su, Y. Q. Lan, *Angew. Chem. Int. Ed.* **2018**, *57*, 9660 – 9664; *Angew. Chem.* **2018**, *130*, 9808 – 9812.
[17] F. L. Li, Q. Shao, X. Q. Huang, J. P. Lang, *Angew. Chem. Int. Ed.* **2018**, *57*, 1888 – 1892; *Angew. Chem.* **2018**, *130*, 1906 – 1910.
[18] Z. B. Liang, C. Qu, W. H. Guo, Y. Q. Zou, Q. Xu, *Adv. Mater.* **2017**, *29*, 1702891.
[19] H. L. Wang, Q. L. Zhu, Y. Q. Zou, Q. Xu, *Chem* **2017**, *2*, 52 – 80.
[20] W. Wang, X. M. Xu, W. Zhou, Z. P. Shao, *Adv. Sci.* **2017**, *4*, 1600371.
[21] D. Sheberla, J. C. Bachman, S. E. Joseph, C. J. Sun, Y. S. Horn, M. Dinca, *Nat. Mater.* **2017**, *16*, 220 – 224.
[22] M. L. Aubrey, B. M. Wiers, S. C. Andrews, T. Sakurai, S. E. ReyesLillo, S. M. Hamed, C. J. Yu, L. E. Darago, J. A. Mason, J. O. Baeg, F. Grandjean, G. J. Long, S. Seki, J. B. Neaton, P. D. Yang, J. R. Long, *Nat. Mater.* **2018**, *17*, 625 – 632.
[23] I. Stassen, N. Burtch, A. Talin, P. Falcaro, M. Allendorf, R. Ameloot, *Chem. Soc. Rev.* **2017**, *46*, 3185 – 3241.
[24] J. A. DeGayner, I. R. Jeon, L. Sun, M. Dinca, T. D. Harris, *J. Am. Chem. Soc.* **2017**, *139*, 4175 – 4184.
[25] P. Q. Liao, J. Q. Shen, J. P. Zhang, *Coord. Chem. Rev.* **2018**, *373*, 22 – 48.
[26] A. J. Clough, J. W. Yoo, M. H. Mecklenburg, S. C. Marinescu, *J. Am. Chem. Soc.* **2015**, *137*, 118 – 121.
[27] B. Wurster, D. Grumelli, D. Hotger, R. Gutzler, K. Kern, *J. Am. Chem. Soc.* **2016**, *138*, 3623 – 3626.
[28] L. Wang, Y. Z. Wu, R. Cao, L. T. Ren, M. X. Chen, X. Feng, J. W. Zhou, B. Wang, *ACS Appl. Mater. Interfaces* **2016**, *8*, 16736 – 16743.
[29] S. L. Zhao, Y. Wang, J. C. Dong, C. T. He, H. J. Yin, P. F. An, K. Zhao, X. F. Zhang, C. Gao, L. J. Zhang, J. W. Lv, J. X. Wang, J. Q. Zhang, A. M. Khattak, N. A. Khan, Z. X. Wei, J. Zhang, S. Q. Liu, H. J. Zhao, Z. Y. Tang, *Nat. Energy* **2016**, *1*, 16184.
[30] J. Duan, S. Chen, C. Zhao, *Nat. Commun.* **2017**, *8*, 15341.
[31] L. Zhao, B. L. Dong, S. Z. Li, L. J. Zhou, L. F. Lai, Z. W. Wang, S. L. Zhao, M. Han, K. Gao, M. Lu, X. J. Xie, B. Chen, Z. D. Liu, X. J. Wang, H. Zhang, H. Li, J. Q. Liu, H. Zhang, X. Huang, W. Huang, *ACS Nano* **2017**, *11*, 5800 – 5807.
[32] F. Z. Sun, G. Wang, Y. Q. Ding, C. Wang, B. B. Yuan, Y. Q. Lin, *Adv. Energy Mater.* **2018**, *8*, 1800584.
[33] D. Senthil Raja, X. F. Chuah, S. Y. Lu, *Adv. Energy Mater.* **2018**, *8*, 1801065.
[34] K. Rui, G. Q. Zhao, Y. P. Chen, Y. Lin, Q. Zhou, J. Y. Chen, J. X. Zhu, W. P. Sun, W. Huang, S. X. Dou, *Adv. Funct. Mater.* **2018**, *28*, 1801554.
[35] Q. Liu, L. S. Xie, G. Du, A. M. Asiri, Y. L. Luo, X. P. Sun, *Inorg. Chem. Front.* **2018**, *5*, 1570 – 1574.
[36] G. T. Hai, X. L. Jia, K. Y. Zhang, X. Liu, J. Yang, C. Tan, Q. Ma, Q. Lu, J. Chen, X. Zhang, Z. Zhang, Z. Y. Wu, G. Wang, *Nano Energy* **2018**, *44*, 345 – 352.
[37] J. Huang, Y. Li, R. K. Huang, C. T. He, L. Gong, Q. Hu, L. Wang, Y. T. Xu, X. Y. Tian, S. Y. Liu, Z. M. Ye, F. Wang, D. D. Zhou, W. X. Zhang, J. P. Zhang, *Angew. Chem. Int. Ed.* **2018**, *57*, 4632 – 4636; *Angew. Chem.* **2018**, *130*, 4722 – 4726.
[38] M. T. Zhao, Y. Huang, Y. W. Peng, Z. Q. Huang, Q. L. Ma, H. Zhang, *Chem. Soc. Rev.* **2018**, *47*, 6267 – 6295.
[39] E. L. Hu, Y. F. Feng, J. W. Nai, D. Zhao, Y. Hu, X. W. Lou, *Energy Environ. Sci.* **2018**, *11*, 872 – 880.
[40] Y. P. Wu, W. Zhou, J. Zhao, W. W. Dong, Y. Q. Lan, D. S. Li, C. H. Sun, X. H. Bu, *Angew. Chem. Int. Ed.* **2017**, *56*, 13001 – 13005; *Angew. Chem.* **2017**, *129*, 13181 – 13185.
[41] J. Jiang, L. Huang, X. M. Liu, L. H. Ai, *ACS Appl. Mater. Interfaces* **2017**, *9*, 7193 – 7201.
[42] F. Yang, G. Xu, Y. B. Dou, B. Wang, H. Zhang, H. Wu, W. Zhou, J. R. Li, B. L. Chen, *Nat. Energy* **2017**, *2*, 877 – 883.
[43] X. F. Lu, P. Q. Liao, J. W. Wang, J. X. Wu, X. W. Chen, C. T. He, J. P. Zhang, G. R. Li, X. M. Chen, *J. Am. Chem. Soc.* **2016**, *138*, 8336 – 8339.
[44] K. He, Z. Cao, R. R. Liu, Y. Miao, H. Y. Ma, Y. Ding, *Nano. Res.* **2016**, *9*, 1856 – 1865.
[45] C. S. Cao, D. D. Ma, Q. Xu, X. T. Wu, Q. L. Zhu, *Adv. Funct. Mater.* **2018**, *28*, 1807418.

Manuscript received: November 29, 2018
Revised manuscript received: January 21, 2019
Version of record online: February 18, 2019

